

# Study of electrospun polyacrylonitrile fibers with porous and ultrafine nanofibril structures: Effect of stabilization treatment on the resulting carbonized structure

Chien-Lin Huang <sup>1</sup>, Tzu-Hsin Wei,<sup>1</sup> Sheng-Yin Peng,<sup>1</sup> Kun-Mu Lee<sup>2,3</sup>

<sup>1</sup>Department of Fiber and Composite Materials, Feng Chia University, Taichung 40724, Taiwan

<sup>2</sup>Department of Chemical and Materials Engineering, Chang Gung University, Taoyuan 33302, Taiwan

<sup>3</sup>Division of Neonatology, Department of Pediatrics, Chang Gung Memorial Hospital, Linkou, Taoyuan 33305, Taiwan

Correspondence to: C.-L. Huang (E-mail: clhuang@mail.fcu.edu.tw)

**ABSTRACT:** Electrospun polyacrylonitrile (PAN)-based carbon nanofibers (CNFs) with high surface area have been of promising interest because of their potential for applications in various fields, especially energy devices. In this study, PAN nanofibers with porous and ultrafine nanofiber structures were prepared by electrospinning PAN/poly(vinyl pyrrolidone) (PVP) immiscible solutions and then selectively removing the PVP component from the electrospun PAN/PVP bicomponent nanofibers. The chemical reaction and microstructure of the PAN fibers with porous and ultrafine nanofibril structures in the stabilization process were investigated. The results revealed the effects of PAN fibers with porous and ultrafine nanofibril structures on the crosslinking reaction, microstructure, and morphology during the stabilization process. According to the *in situ* Fourier transform infrared spectroscopy results, the intermolecular and intramolecular reactions of the nitrile group for the PAN fibers with ultrafine nanofibril structures exhibited slower reaction rates than those for the neat PAN fibers during stepwise and isothermal heating. Selecting a good stabilization temperature for ultrafine PAN-crosslinked nanofibrils can enhance the surface area and carbonized structure of CNFs. The possible applications of CNFs with porous and ultrafine nanofibril structures in supercapacitors were also evaluated. © 2019 Wiley Periodicals, Inc. *J. Appl. Polym. Sci.* **2019**, *136*, 48218.

**KEYWORDS:** carbon nanofiber; electrode; electrospinning; polyacrylonitrile; stabilization; ultrafine nanofibril

Received 12 October 2018; accepted 14 June 2019

DOI: 10.1002/app.48218

## INTRODUCTION

Carbon materials have been used as supercapacitor electrode material with promising interest as they have a unique combination of physicochemical properties, such as high conductivity, a high surface-area range, good corrosion resistance, high temperature stability, processability and compatibility in composite materials, and relatively low cost.<sup>1</sup> Moreover, carbon materials with nanostructures can significantly increase the interface areas between solids and liquids or solids and gases, which will reduce the electron or ion diffusion distance and improve electrochemical performance. According to the literatures,<sup>2</sup> the capacitance of electric double-layer capacitors at each electrode interface can be used in the following equation:

$$\text{Capacitance} = \frac{\epsilon A_e}{4\pi t} \quad (1)$$

where  $\epsilon$  is the dielectric constant of the electrical double-layer region,  $A_e$  is the surface area of the electrode, and  $t$  is the thickness of the

electrical double layer. Therefore, the higher surface area of the carbon electrodes can lead to higher capacitance. Recently, one-dimensional carbon nanomaterials have shown promise from developers of energy storage devices because they have better electrochemical properties than zero-dimensional carbon nanomaterials.<sup>3</sup> Therefore, preparing polyacrylonitrile (PAN)-based carbon nanofibers (CNFs) with high surface areas has been of immense interest. Furthermore, CNFs with high surface areas also play an important role in electrode materials for other energy storage devices, such as lithium-ion batteries, lithium–air batteries, lithium–sulfur batteries, and sodium-ion batteries.<sup>3</sup>

Electrospinning has attracted enormous attention in the past two decades as a method for fabricating one-dimensional polymeric nanofibers. Electrospun fiber mats have been widely explored in various applications, such as energy devices, filtration, tissue engineering, and biosensors because of their high surface area-to-volume ratio, high porosity, diverse nanostructures, and assembly morphologies.<sup>4</sup> More importantly, electrospinning allows facile and cost-effective preparation of continuous nanofibers. Thus,

Additional Supporting Information may be found in the online version of this article.

© 2019 Wiley Periodicals, Inc.

PAN-based CNFs prepared via electrospinning could increase the functional properties of fibers for advanced applications, particularly energy storage systems. For a supercapacitor application, the specific surface area of CNFs is an important issue. There are two major routes to increase the specific surface area of CNFs. First, the specific surface area of CNFs can be increased by decreasing the diameter of the CNFs. Second, the specific surface area of CNFs can be increased due to the porous structure in the CNFs.

PAN fibers with porous structures can be prepared via electrospinning with various routes.<sup>3,5</sup> Among these methods, PAN fibers with porous structures can be appropriately produced by electrospinning immiscible polymer solutions (polymer blend solutions), such as PAN/poly(methyl methacrylate) (PMMA), PAN/poly(vinyl pyrrolidone) (PVP), or PAN/PEO solutions. Zhang and Hsieh<sup>6</sup> showed that PAN fibers with porous structures could be produced via an electrospinning PAN/poly(ethylene oxide) (PEO) bicomponent solution and then selectively removing the PEO component via water extraction. Zhang *et al.*<sup>7</sup> also reported that PAN fibers and CNFs with porous structures were produced via electrospinning PAN/PVP bicomponent solution and then selectively removing the PVP component via water extraction. The PAN/PVP weight ratios were prepared from 80/20 to 44/56. Moreover, the Brunauer–Emmett–Teller (BET) surface area of the PAN fibers and CNFs with porous structures was increased as the PVP content increased. Sun *et al.*<sup>8</sup> prepared the electrospun PAN fiber with ultrafine nanofibril structures via supercritical drying. They also demonstrated that the BET surface area of the PAN fibers and CNFs with ultrafine nanofibril structures have large surface area with or without carbonization. Niu *et al.*<sup>9</sup> demonstrated that electrospun PAN/PVP blend nanofibers and PAN/PVP side-by-side nanofibers with carbonization process would form the interfiber connections to reduce the resistivity of CNF mats. Peng *et al.*<sup>10</sup> demonstrated that porous CNFs could be prepared via electrospinning a PAN/poly(AN-co-PMMA) solution and pyrolyzing the copolymer phase during the thermal oxidation process to form CNFs with porous structures after the carbonization process. Shilpa *et al.*<sup>11</sup> also reported that CNFs with a porous and hollow structure could be prepared via electrospinning a PAN/PMMA solution and selectively removing the PMMA component via the pyrolysis process. However, the electrical conductivity of CNFs with porous structures is lower than that of neat CNFs because the effective conductive length of the electrons in CNFs with porous structures will be longer than in neat CNFs.

On the other hand, the diameter of electrospun fibers via a single polymer solution is rarely smaller than 50 nm (ultrafine nanofibrils) due to limitations of the electrospinning process. However, Bognitzki *et al.*<sup>12</sup> demonstrated that porous polymer nanofiber and ultrafine polymer nanofibrils can be prepared via immiscible polymer solutions in which one component is removed selectively from the fibers. Lee *et al.*<sup>13</sup> demonstrated electrospun PCL/P3HT composite fibers with continuous P3HT fibrils embedded inside. The small P3HT domains in the concentrated PCL/P3HT solution are highly stretched during electrospinning and form fibrils with small diameters. However, there is little information available on electrospun PAN-based CNF with an ultrafine nanofibril structure.

PAN fiber can be converted to carbon fibers via thermal treatment. During thermal treatment, PAN fibers usually go through

stabilization and carbonization processes.<sup>14–16</sup> For the stabilization process at 200–300 °C, the chemical structure of PAN will be changed with cyclization, dehydrogenation, aromatization, oxidation, and crosslinking reactions in air atmospheres to form a ladder structure. After stabilization, PAN is carbonized at 700–1300 °C in nitrogen atmospheres to form a turbostratic structure. Cipriani *et al.*<sup>17</sup> reported that the formation of triazine with an intermolecular reaction involving three nitriles of three different PAN chains is responsible for the crosslinking. Thus, the key reactions in the stabilization process are intermolecular and intramolecular nitrile crosslink reactions, which change the chemical structure of PAN to form a ladder structure due to cyclization of the nitrile groups. These groups can promote the formation of a conjugated carbon structure in the carbonization process. PAN fibers can overheat or fuse at higher stabilization temperatures. On the other hand, PAN fibers can have incomplete stabilization, which results in poor carbon fiber properties, at lower stabilization temperatures. Therefore, selecting the appropriate stabilization temperature is important for PAN fibers to convert to carbon fibers with better carbonized structures. Moskowitz *et al.*<sup>18</sup> showed that the PAN prepared via free radical solution polymerization has a larger extent of stabilization at lower temperature regions than that prepared via reversible addition–fragmentation chain transfer polymerization. Lai *et al.*<sup>19</sup> demonstrated that the PAN chains in the as-electrospun PAN nanofibers are less oriented along the fiber than those in stretched PAN nanofibers. Furthermore, the CNF bundles in the postspinning stretching process have better mechanical properties than those without any stretching process. Lian *et al.*<sup>20</sup> also reported that the cyclization index of highly stretched PAN fiber is lower than that of PAN fibers without any stretching process at 180 °C.

However, to the best of our knowledge, the effect of the chemical reactions and the microstructure of electrospun PAN fibers with porous and ultrafine nanofibril structures during stabilization processes have not yet been reported. In this study, the phase separation PAN/PVP solutions with various PAN/PVP weight ratios, especially, a low PAN content, were prepared for electrospinning. After removing most of the PVP components with hot water and sodium hypochlorite from the PAN/PVP nanofibers, PAN fiber with porous and ultrafine nanofibril structures could be obtained. In order to reveal the influence of the carbonized structures during the stabilization process for PAN fibers with porous and ultrafine nanofibril structures, the CNFs in this study were not oxidation etched with oxidizing gases (activation process) to form porous structures.<sup>3,5</sup> Therefore, the PAN fibers with porous and ultrafine nanofibril structures were heated up to 330 °C in a hot stage using air atmospheres with *in situ* Fourier transform infrared (FTIR) spectroscopy to reveal the intermolecular and intramolecular nitrile crosslink reactions. According to the *in situ* FTIR results, the PAN fibers with ultrafine nanofibril structure for stabilization at 260 °C were more stable and could convert PAN to a ladder crosslinking compound than that at 320 °C. After stabilization and carbonization of the PAN fibers with porous and ultrafine nanofibril structures, CNFs with nanoporous and ultrafine fibril structures were also obtained. The PAN fibers with porous and ultrafine nanofibril structures not only affected the chemical reaction but also

affected the morphologies during stabilization. Therefore, the surface area of the PAN fibers with porous and ultrafine nanofibril structures was also affected after carbonization. In addition, the electrochemical property of the CNF mats was evaluated.

## EXPERIMENTAL

### Materials and PAN/PVP Solution Preparation

The PAN was purchased from the Scientific Polymer Products, Inc. (Ontario, NY, USA), and the weight-average molecular weight of the PAN was determined to be  $150,000 \text{ g mol}^{-1}$ . The PVP was purchased from the ARCOS (Morris Plains, NJ, USA), and the weight-average molecular weight of the PVP was determined to be  $1,300,000 \text{ g mol}^{-1}$ . The dimethylformamide (DMF) was purchased from Echo Chemical Co. (Miaoqi, Taiwan). To prepare a PAN/PVP solution with varying PAN/PVP weight ratios (25/75, 50/50, and 75/25), preweighed PAN and PVP powders were added to a DMF solvent and vigorously stirred for several hours. The total polymer concentration was 8 wt %, and a PAN/PVP solution was then obtained. In the present study, a 25/75 sample designation indicated the PAN-to-PVP weight ratio.

### Electrospinning, Stabilization, and Carbonization Process

The prepared solutions were subjected to room temperature electrospinning, wherein the nozzle size was  $D_i/D_o/\text{length} = 0.69 \text{ mm}/1.09 \text{ mm}/4 \text{ cm}$ , and  $D_i$  and  $D_o$  were the inner and outer nozzle diameters, respectively. The prepared solutions were delivered by a syringe pump (Cole-Parmer, Vernon Hills, IL, USA) to the nozzle at a controlled flow rate ( $Q$ ). A high electrical voltage ( $V$ ) was applied to the spinneret using a high-voltage source (MECC, HVU-40P100, Fukuoka, Japan) to provide a sufficient electric field for electrospinning. To construct a needle-to-plate electrode configuration, an aluminum board ( $30 \times 30 \text{ cm}^2$ ) was used as the collector for the electrospun fibers at a fixed tip-to-collector distance ( $H$ ) of 14 cm. The electrospun PAN/PVP nanofibers with varying PAN/PVP weight ratios were immersed in hot water and a sodium hypochlorite solution (8000 ppm) to remove the PVP components, and then washed in deionized water for five times with ultrasonic treatment for 5 min. Notably that the absence of any sodium hypochlorite (O—Cl—) absorbance peaks at  $975 \text{ cm}^{-1}$  of the FTIR spectra, which were assigned to hypochlorous acid vibration.<sup>21</sup> Thus, no residual sodium hypochlorite was detected in the PAN fibers with porous and ultrafine nanofibril. After washing, the PAN fibers with porous and ultrafine nanofibril were dried in a vacuum oven until the residual water was removed. The PAN fibers with porous and ultrafine nanofibril structures were obtained. The PAN fibers with porous and ultrafine nanofibril structures were put through the stabilization process in air at  $320 \text{ }^\circ\text{C}$  for 1 h at a heating rate of  $1 \text{ }^\circ\text{C min}^{-1}$  and then the carbonization process using a nitrogen airflow at  $900 \text{ }^\circ\text{C}$  for 1 h at a heating rate of  $5 \text{ }^\circ\text{C min}^{-1}$  in a tube furnace. CNF was then obtained. Sample codes of the PAN/PVP composite fibers obtained and the resulting fibers with the removed PVP component and carbonization process are given in Table I.

### Morphology and Characterization of Fibers

The morphology of the fibers was observed using a scanning electron microscope (SEM, Hitachi S4100, Krefeld, Germany). The fiber diameters were measured from a collection of  $\sim 200$  fibers, from

which the average diameter ( $d_f$ ) was determined. FTIR measurements were performed using a PerkinElmer FTIR spectrometer (Spectrum Two, Waltham, MA, USA) equipped with a Mettler heating stage (HT82) for temperature control. A total of 32 scans with a  $2 \text{ cm}^{-1}$  resolution were obtained for each spectrum. The wide-angle X-ray diffraction (WAXD) intensity profiles of the PAN nanofibers and CNF mats composite films were obtained using a Bruker diffractometer (NANOSTAR Universal System, Cu  $K_\alpha$  radiation, Billerica, MA, USA). The stabilization of the PAN nanofibers was investigated using a TA differential scanning calorimetry (DSC) Q20 (New Castle, DE, USA) under a nitrogen atmosphere. The samples were heated to  $340 \text{ }^\circ\text{C}$  at a rate of  $10 \text{ }^\circ\text{C min}^{-1}$ .

The microstructure in the CNF-UF samples was examined with transmission electron microscope (TEM) (JOEL JEM-2010, Peabody, MA, USA) operated at 200 kV. The CNF-UF samples were embedded in Embed-812 (Electron Microscopy Sciences, Hatfield, PA, USA). The film was then prepared by sectioning the embedded CNF-UF samples at room temperature with an Ultracut UCT (Leica, Wetzlar, Germany) microtome, and the ultrathin films with approximately 50 nm thickness were observed using TEM. Electrical conductivity measurements were performed using a GW INSTEK GDM-8261A multimeter. The standard four-probe technique was applied to reduce the effects of contact resistance with applied voltage between 1 and 10 V. Thermogravimetric analysis (TGA) was performed on a TGA 2050 (TA Instruments, New Castle, DE, USA) apparatus under a nitrogen flow ( $90 \text{ mL min}^{-1}$ ) from 25 to  $800 \text{ }^\circ\text{C}$  at a heating rate of  $10 \text{ }^\circ\text{C min}^{-1}$ . The weight of the samples used was approximately 5 mg. The surface areas of CNF samples were analyzed on an ASAP 2020 (Micromeritics Instruments, Norcross, GA, USA) according to the BET equation.

The electrochemical capacitance of the CNF mats was determined by the cyclic voltammetry (CV) method on an electrochemistry workstation (CH Instruments; CHI 600, Austin, TX, USA). CNF mats ( $10 \times 10 \text{ mm}^2$ ) with a graphite plate ( $30 \times 15 \times 2 \text{ mm}^3$ ), Ag/AgCl, and a Pt foil ( $1 \times 1 \text{ cm}^2$ ) were used as the working, reference, and counter electrodes, respectively.<sup>9</sup> An  $\text{H}_2\text{SO}_4$  (1.0 M) aqueous solution was used as the electrolyte solution in the three electrode cell. The measurement was carried out at  $25 \text{ }^\circ\text{C}$  with a scan range of 0 to 1 V and a scan rate of  $50 \text{ mV s}^{-1}$ .

## RESULTS AND DISCUSSION

### Thermal Properties of PAN Fibers with Porous and Ultrafine Nanofibril Structures

Figure 1(a–e) shows the SEM images of the neat PAN nanofibers and neat CNFs. The  $d_f$  of PAN nanofibers, PAN/PVP nanofibers, and CNFs are listed in Table I. The  $d_f$  of the neat PAN nanofiber was  $420 \pm 58 \text{ nm}$ . The  $d_f$  of the neat CNF nanofiber was  $248 \pm 36 \text{ nm}$ . Less crosslinked morphologies were observed in the neat CNF. However, the fused feature can also be observed in the neat CNFs. Two PAN fibers would merge together when the surfaces of two neat PAN fibers are in contact with each other. Figure S1(a–c) shows SEM images of the PAN/PVP bicomponent fiber products collected from the electrospinning of the PAN/PVP solutions with varying PAN/PVP weight ratios. For the 8 wt % polymer concentration, all electrospun PAN/PVP bicomponent fibers with varying PAN/PVP weight ratios were bead-free fibers.

**Table I.** Sample Codes, Average Diameter ( $d_f$ ), and Short Axis of Surface Pores ( $P_s$ ) of PAN/PVP Composite Fibers Obtained and the Resulting Fibers with the Removed PVP Component and Carbonization Process

Electrospinning solution polymer composition (PAN/PVP)	As-spun PAN/PVP nanofibers		Porous PAN nanofibers (removed PVP component)			Porous carbon nanofibers		
	Sample code	$d_f$ (nm)	Sample code	$d_f$ (nm)	$P_s$ (nm)	Sample code	$d_f$ (nm)	$P_s$ (nm)
100/0	PAN/PVP 100/0	420 ± 58	neat PAN	420 ± 58	—	neat CNF	248 ± 36	—
75/25	PAN/PVP 75/25	276 ± 28	PAN-P1	200 ± 27	10.8 ± 2.7	CNF-P1	153 ± 23	29.0 ± 10.0
50/50	PAN/PVP 50/50	221 ± 35	PAN-P2	195 ± 33	16.1 ± 3.7	CNF-P2	152 ± 26	—
25/75	PAN/PVP 25/75	167 ± 23	PAN-UF	16 ± 3	—	CNF-UF	117 ± 16	—

The  $d_f$  of PAN/PVP 75/25, PAN/PVP 50/50, and PAN/PVP 25/75 fibers were 276 ± 28 nm, 221 ± 35 nm, and 167 ± 23 nm, respectively. The PAN/PVP bicomponent fibers with varying PAN/PVP weight ratios were put through selective removal of the PVP component via immersion in hot water with 8000 ppm sodium hypochlorite. After removing most of the PVP components with hot water and sodium hypochlorite from the PAN/PVP nanofibers, the weight loss ratios of PAN/PVP 75/25, PAN/PVP 50/50, and PAN/PVP 25/75 were 26 ± 1, 48 ± 3, and 77 ± 1%, respectively. Hence, only the weight loss ratio of PAN/PVP 50/50 nanofibers was slightly smaller than the prepared ratio of the PVP content of PAN/PVP 50/50 nanofibers after washing. Moreover, the deviation in the weight loss ratio of PAN/PVP 25/75, PAN/PVP 50/50, and PAN/PVP 75/25 nanofibers may have been due to the water absorption of PVP content and operation inaccuracy. This result indicated that the residue of PVP content for PAN-P1, PAN-P2, and PAN-UF nanofibers can be very small.

Figure 1(b–d) shows the SEM images of the PAN fibers with porous and ultrafine nanofibril structures. Continuous residual fibers were obtained after the PVP components were removed selectively from the fibers. The  $d_f$  and short axis of surface pores ( $P_s$ ) of PAN fibers with porous and ultrafine nanofibril structures are also listed in Table I. The PAN-P1 and PAN-P2 nanofibers developed a porous surface structure. Surface pores were observed with short axis dimensions in the order of 10.8 ± 2.7 nm and 16.1 ± 3.7 nm in the PAN-P1 and PAN-P2 nanofibers, respectively, whereas the  $d_f$  of the PAN-P1 and PAN-P2 nanofibers were 200 ± 27 nm and 195 ± 33 nm, respectively. PAN-UF nanofibers could be observed with ultrafine nanofibrils at an  $d_f$  of 16 ± 3 nm inside the PAN-UF nanofibers after the PVP component was removed selectively from the fibers. Furthermore, the outer shell  $d_f$  of the PAN-UF nanofibers was 167 ± 21 nm. The SEM images of the cross sections of PAN-UF nanofiber mats are shown in Figure S2. The ultrafine PAN nanofibril structure was found on the PAN-UF nanofiber mat surface and inside the PAN-UF nanofiber mats. The phase-separating domains of the PAN/PVP 25/75 solution were stretched into string phase under shear flow during electrospinning. The string phases became ultrafine nanofibrils after the selective removal of the PVP component from the fibers. However, the PVP domains of the PAN/PVP 75/25 and PAN/PVP 50/50 solution were stretched into ellipsoidal phase during electrospinning. The ellipsoidal domains acquired porous

structures in PAN-P1 and PAN-P2 fibers after the selective removal of the PVP component from the fibers. Thus, the PAN fibers with porous structures provided more random orientation PAN chains than those with ultrafine nanofibril structures for fiber shrinkage during the selective removal of the PVP component via water extraction. Nevertheless, the effects of the PVP molecular weight in PAN/PVP phase separation solution properties could affect the PAN fiber morphologies after selective removal of the PVP component from the fibers. This issue was beyond the scope of this study and deserved future work.

The PAN fibers with porous and ultrafine nanofibril structures were heated to 320 °C in air for 1 h at a heating rate of 1 °C min<sup>-1</sup> for the stabilization process, and then heated to 900 °C in a nitrogen atmosphere for 1 h at a heating rate of 5 °C min<sup>-1</sup> for the carbonization process. This caused the fiber color to change from white to black, and the porous and ultrafine nanofibril structures were changed dramatically due to thermal shrinkage. Figure 1(g,h) shows the SEM images of the PAN fibers with porous and ultrafine nanofibril structures after the carbonization process. The  $d_f$  and  $P_s$  of CNFs with porous structures are also listed in Table I. When the PAN-P1 nanofibers were treated with the stabilization and carbonization processes, the CNF-P1 appeared to have an ellipse-shaped porous structure with a short axis of 29.0 ± 10.0 nm, and the  $d_f$  of CNF-P1 was 153 ± 23 nm. When the PAN-P2 nanofibers were treated with the stabilization and carbonization processes, the CNF-P2 appeared to have a regular undulating structure with a  $d_f$  of 152 ± 26 nm. Based on the SEM images, the CNF-P2 showed a regular undulating structure. Moreover, pore structures remained on the CNF-P2 surface, but the pore size of CNF-P2 was difficult to determine because of the regular undulating structure. When the PAN-UF nanofibers were treated with the stabilization and carbonization processes, the CNF-UF also appeared to have a regular undulating structure with a  $d_f$  of 117 ± 16 nm. Based on the results in Table I, the  $d_f$  values of the CNF-P1 and CNF-P2 were smaller than those of PAN-P1 and PAN-P2, respectively, while the  $d_f$  value of CNF-UF was also smaller than the outer shell  $d_f$  value of the PAN-UF. Moreover, the  $d_f$  value of the neat CNF was smaller than that of the neat PAN due to thermal shrinkage during PAN crosslinking and cyclization reactions. It was noteworthy that the ultrafine PAN nanofibrils disappeared during carbonization. If the PAN fibers with porous and ultrafine nanofibril structures were utilized as a supercapacitor electrode precursor, it would be important to

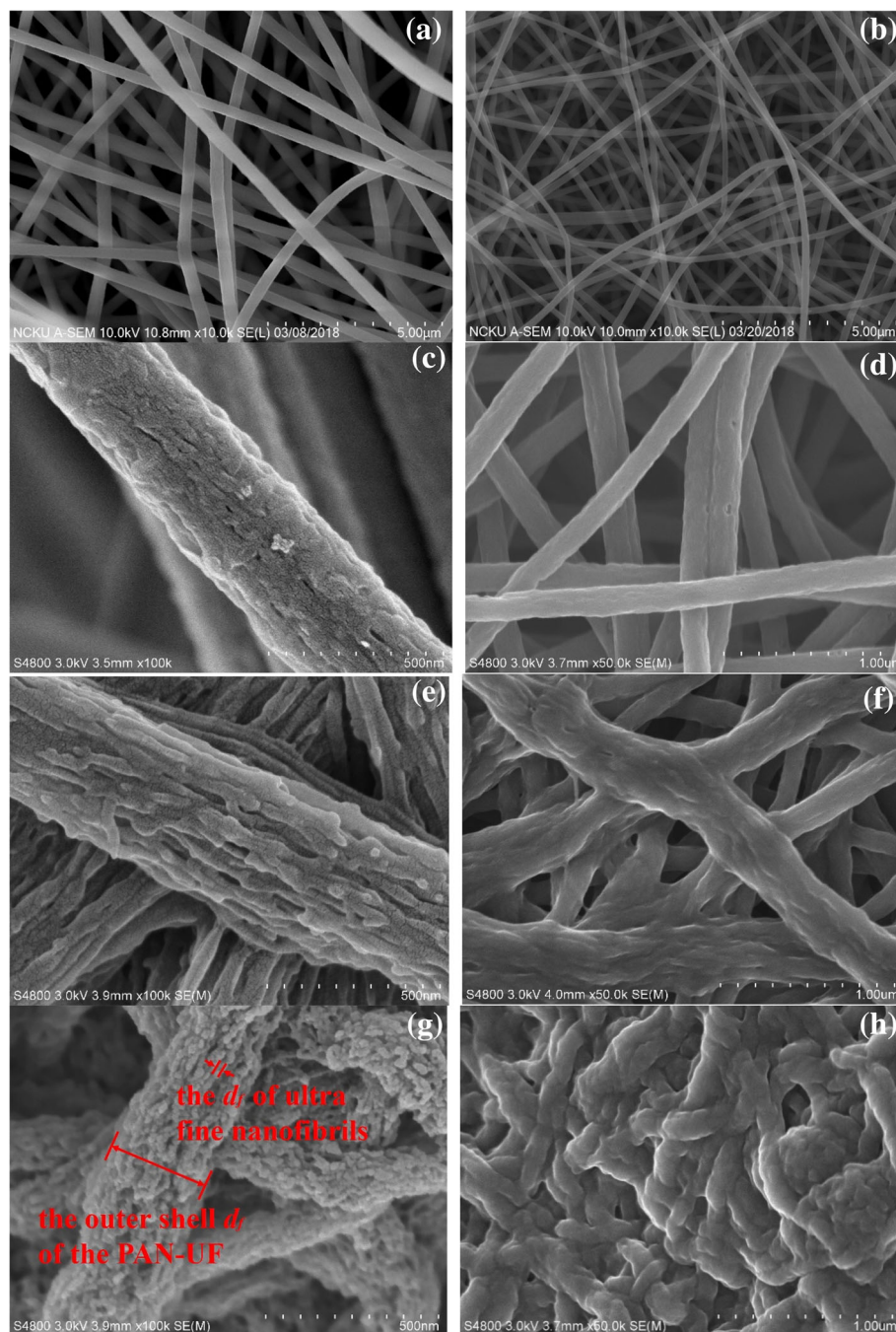


**Figure 1.** SEM images of (a) neat PAN nanofibers, (b) PAN-P1 nanofibers, (c) PAN-P2 nanofibers, (d) PAN-UF nanofibers, (e) neat CNFs, (f) CNFs-P1, (g) CNFs-P2, and (h) CNFs-UF. [Color figure can be viewed at [wileyonlinelibrary.com](http://wileyonlinelibrary.com)]

keep the porous and ultrafine nanofibril structures during the stabilization and carbonization processes to enhance the surface area of CNF. However, most of the porous and ultrafine nanofibril structures would disappear after carbonization. This implied that the PAN chains in the PAN fibers with porous and ultrafine nanofibril structures would relax by thermal shrinkage during thermal heating. In order to reduce the thermal relaxation of the PAN chains, the selection of an appropriate stabilization temperature for the PAN-crosslinked fibers was important. Therefore, TGA, DSC, and *in situ* FTIR spectroscopy was used to study the intermolecular and intramolecular cyclization reactions in the

PAN fibers with porous and ultrafine nanofibril structures during stabilization.

Figure 2(a) shows the TGA curves of the PAN fibers with porous and ultrafine nanofibril structures in the nitrogen atmospheres at  $10\text{ }^{\circ}\text{C min}^{-1}$ . The thermal degradation in nitrogen atmosphere of the neat PAN, PAN-P1, PAN-P2, and PAN-UF nanofibers began at 289, 294, 293, and 287  $^{\circ}\text{C}$ , respectively. According to the literature,<sup>18,22,23</sup> the weight loss between 270 and 300  $^{\circ}\text{C}$  in the TGA plots results from cyclization and dehydrogenation, whereas the weight loss between 300 and 450  $^{\circ}\text{C}$  in the TGA plots is

caused by the release of small impurities from the ladder structure. In addition, the plateau between 450 and 800 °C of the PAN fibers in TGA plots were form the stabilized structure. In nitrogen atmosphere, the residue of the neat PAN, PAN-P1, PAN-P2, and PAN-UF nanofibers left at 800 °C is 33.3, 30.9, 28.4, and 34.6 wt %, respectively. The plateau between 450 and 800 °C of PAN-P1, PAN-P2, and PAN-UF nanofibers was lower than that of the neat PAN nanofibers. This indicated that the thermal stability of the PAN fibers with porous and ultrafine nanofibril structures was lower than that of the neat PAN nanofibers.

Figure 2(b) shows the DSC heating traces of the PAN fibers with porous and ultrafine nanofibril structures in the nitrogen atmosphere at a heating rate of 10 °C min<sup>-1</sup>. Because PVP can easily absorb water from the air, the plasticizer effect of the absorbed water results in an endothermic peak ( $T_a$ ) at 105.6 °C. Kim<sup>24</sup> reported a similar result. The  $T_a$  of the PAN fibers with porous and ultrafine nanofibril structures could be still observed. This indicated that there was still some PVP content in the PAN fibers with porous and ultrafine nanofibril structures after the PVP components were removed. The  $T_a$  of PAN-P1, PAN-P2, and PAN-UF nanofibers was 84.0, 128.5, and 123.4 °C, respectively. The neat PAN fibers showed a very strong exothermic peak ( $T_c$ ) at about

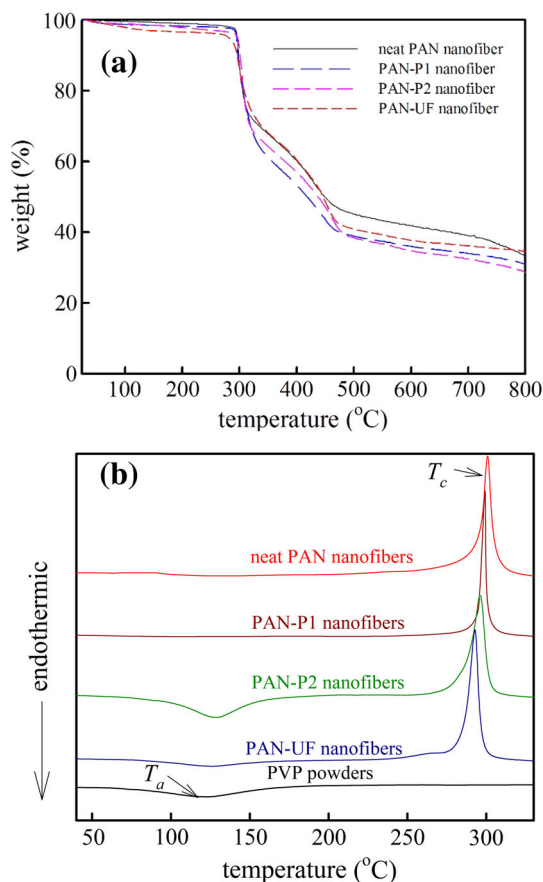


**Figure 2.** (a) TGA curves and (b) DSC heating traces of the PAN fibers with porous and ultrafine nanofibril structures in nitrogen atmospheres at 10 °C min<sup>-1</sup>. [Color figure can be viewed at [wileyonlinelibrary.com](http://wileyonlinelibrary.com)]

300.8 °C from the cyclization reaction of PAN. The  $T_c$  of PAN-P1, PAN-P2, and PAN-UF nanofibers was 299.2, 296.1, and 292.8 °C, respectively. However, previous studies<sup>19,25</sup> indicated that such a thermochemical reaction at 278 and 309 °C would likely be related to the intramolecular and intermolecular reaction of nitrile groups in the PAN macromolecules with extended chain conformations, respectively. The  $T_c$  of the PAN fibers with porous and ultrafine nanofibril structures decreased with the increase in the PVP content. This result implied that the microstructure of the PAN fibers with porous and ultrafine nanofibril structures could affect the cyclization of PAN. However, the dehydrogenation, radiation, intermolecular and intramolecular cyclization, and oxidation reactions would occur during the stabilization process. In addition, TGA and DSC were heated in nitrogen atmospheres, but most of the stabilization process of PAN fibers was heated in air atmospheres. The stabilization process of the PAN nanofibers was difficult to observe via DSC measurements only, therefore, *in situ* FTIR spectroscopy was used to reveal the complex stabilization reactions during heating.

### **In Situ FTIR Spectroscopy of PAN Fibers with Porous and Ultrafine Nanofibril Structures**

Figure 3(a) shows the FTIR spectra of the neat PAN nanofibers during stepwise heating to 330 °C. According to the literatures,<sup>26–28</sup> the absorbance bands at 2936, 2240, and 1453 cm<sup>-1</sup> are associated with the CH<sub>2</sub> asymmetric stretching, nitrile symmetric stretching, and CH<sub>2</sub> bending signals of PAN, respectively. Moreover, prior to heating, broad absorbance bands at approximately 3680–3200 cm<sup>-1</sup> attributed to the water absorption of PAN chains and well-defined absorbance bands at 1625 cm<sup>-1</sup> assigned to C=O of the DMF solvents were detected. When the temperature was increased to 100 °C, the absorbance bands at 3680–3200 cm<sup>-1</sup> and 1625 cm<sup>-1</sup> disappeared. When the temperature was increased to 180 °C, the absorbance bands at 2240 cm<sup>-1</sup> decreased gradually, resulting from radiation of the nitrile group. When the temperature was increased to 220 °C, the absorbance bands at 1576 cm<sup>-1</sup> increased gradually which was related to the formation of imine.<sup>18,29</sup> This indicated either intermolecular or intramolecular reactions of the nitrile group with adjacent nitrile, which formed a ladder structure.<sup>14,30</sup> When the temperature was increased to 240 °C, the increased absorption peak at 1660 cm<sup>-1</sup> confirmed the presence of C=O species and indicated an oxidation reaction during the stabilization process. Furthermore, when the temperature was increased to 250 °C, the increase absorption peak at 804 cm<sup>-1</sup> confirmed the formation of the triazine ring.<sup>17,30</sup> These absorbance changes, which were consistent with previous findings on the stabilization process, revealed the intermolecular and intramolecular reactions of the nitrile group.<sup>17</sup>

Figure 3(b–d) shows the FTIR spectra of the PAN-UF, PAN-P1, and PAN-P2 nanofibers during stepwise heating. A similar increase in the absorbance bands was also observed in the PAN-UF, PAN-P1, and PAN-P2 nanofibers with the increased temperature. For all the PAN fibers with porous and ultrafine nanofibril structures, well-defined absorbance bands at 1682 cm<sup>-1</sup> assigned to C=O were detected.<sup>7</sup> Upon heating, the absorbance band at 1682 cm<sup>-1</sup> still appeared. This indicated that the absorbance band at 1682 cm<sup>-1</sup> was related to the PVP molecules, not the DMF solvent. There were still some PVP molecules in the PAN-UF, PAN-P1, and PAN-P2 nanofibers after removing the PVP component.

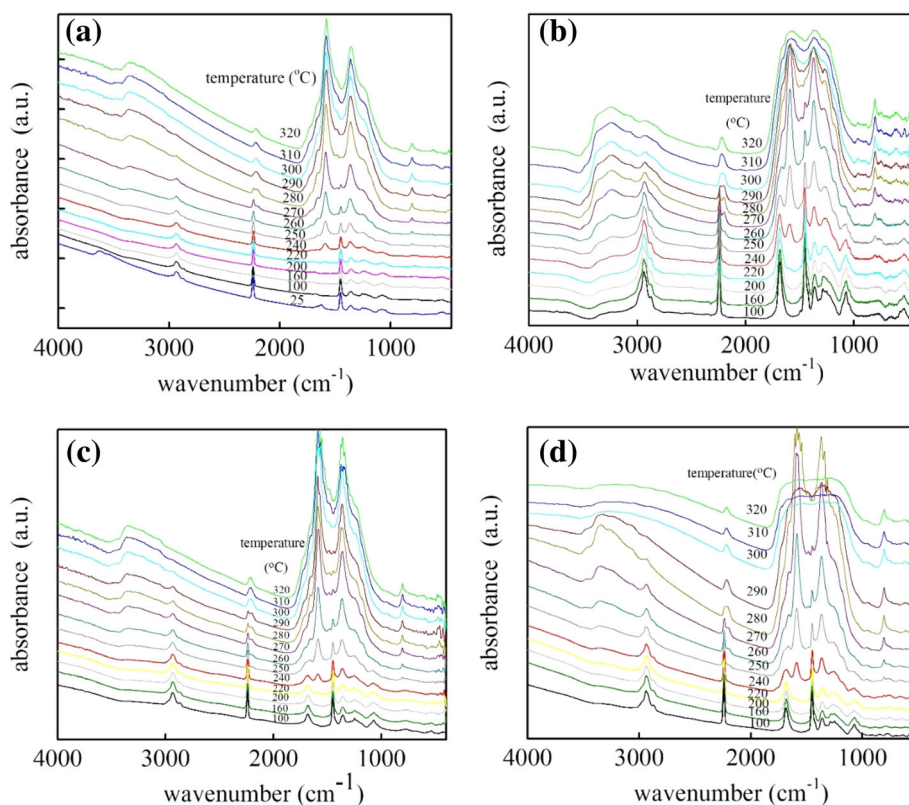


**Figure 3.** FTIR spectra of (a) neat PAN nanofibers, (b) PAN-UF nanofibers, (c) PAN-P1 nanofibers, and (d) PAN-P2 during stepwise heating to 330 °C in air atmospheres at 1 °C min<sup>-1</sup>. [Color figure can be viewed at [wileyonlinelibrary.com](http://wileyonlinelibrary.com)]

This result was consistent with the DSC results. When the temperature was increased to 220 °C, the absorption band of the PAN-UF nanofibers at 2240 cm<sup>-1</sup> began to decrease, while the absorption band of imine, which was slightly shifted to 1587 cm<sup>-1</sup>, began to increase and then decrease at 280 °C. The absorption bands of the triazine ring, which was slightly shifted to 800 cm<sup>-1</sup>, began to increase as the temperature was increased to 240 °C. For the PAN-P1 and PAN-P2 nanofibers, the absorption bands at 2240 cm<sup>-1</sup> began to decrease as the temperature was increased to 180 °C. When the temperature was increased to 240 °C, the absorption bands at 803 cm<sup>-1</sup> began to increase. Moreover, when the temperature was increased to 220 °C, the absorption band at 1587 cm<sup>-1</sup> began to increase. However, the absorption peak of the PAN-P2 nanofibers at 1587 cm<sup>-1</sup> began to decrease at 290 °C. These results indicated that the dehydrogenation, radiation, and intermolecular reactions of the nitrile group for the PAN fibers with porous and ultrafine nanofibril structures exhibited lower starting reaction temperatures than those for the neat PAN nanofibers. The ladder structure of the crosslinked PAN chains for the PAN fibers with porous and ultrafine nanofibril structures could be easily broken down at a higher temperature.

Figure S3 shows magnifications of the range between 2350 and 2100 cm<sup>-1</sup> of the FTIR spectra of the neat PAN, PAN-UF, PAN-P1, and PAN-P2 nanofibers. Variations of the absorption bands between 2240 and 2190 cm<sup>-1</sup> could be observed clearly as the temperature increased. Figure 4(a) shows the variations in the absorbance band of the neat PAN, PAN-P1, PAN-P2, and PAN-UF nanofibers with temperature during stepwise heating. The absorption bands at 2240 cm<sup>-1</sup>

decreased and gradually shifted to 2230 cm<sup>-1</sup> because the nitrile group was transferred to the double bond conjugated nitrile.<sup>17,28</sup> The absorption bands of the neat PAN, PAN-P1, PAN-P2, and PAN-UF nanofibers shifted to 2230 cm<sup>-1</sup> at 290, 300, 285, and 300 °C, respectively. The PAN-UF nanofibers had a higher temperature when the absorption bands shifted to 2230 cm<sup>-1</sup> than the neat PAN nanofibers. Moreover, the absorption band at 2190 cm<sup>-1</sup> gradually shifted to 2220 cm<sup>-1</sup> due to isolated nitriles or imine groups bonded with an aromatic structure [conjugated (2210 cm<sup>-1</sup>) and  $\beta$ -amino (2190 cm<sup>-1</sup>) nitrile groups].<sup>17,28</sup> The temperature for the bands between 2190 and 2220 cm<sup>-1</sup> of the PAN-UF nanofibers to appear was 200 °C, which was lower than those of the neat PAN, PAN-P1, and PAN-P2 nanofibers, whereas the bands between 2190 and 2220 cm<sup>-1</sup> of the neat PAN, PAN-P1, and PAN-P2 nanofibers shifted higher than that of the PAN-UF nanofiber at the lower temperature region. In order to study the extent of the radiation reaction of the nitrile group and the aromatization of the ring of the ladder structure, the area of the absorbance band between 2240 and 2190 cm<sup>-1</sup> required further analysis. However, according to the literature,<sup>28</sup> there are three peaks in the absorbance band between 2240 and 2190 cm<sup>-1</sup>. Thus, given the acquired FTIR spectra profile, peak deconvolution was required to estimate the area of the absorbance band between 2240 and 2190 cm<sup>-1</sup>. The areas of the 2240–2230 and 2220–2190 cm<sup>-1</sup> bands were fitted with a Gaussian–Lorentzian area function. Moreover, the areas of the 2220–2190 cm<sup>-1</sup> bands included both conjugated (2210 cm<sup>-1</sup>) and  $\beta$ -amino (2190 cm<sup>-1</sup>) nitrile groups.

Figure 4(b) shows the normalized area of the absorbance band between 2240 and 2230 cm<sup>-1</sup> ( $A_{2240}$ ) of the neat PAN, PAN-P1,

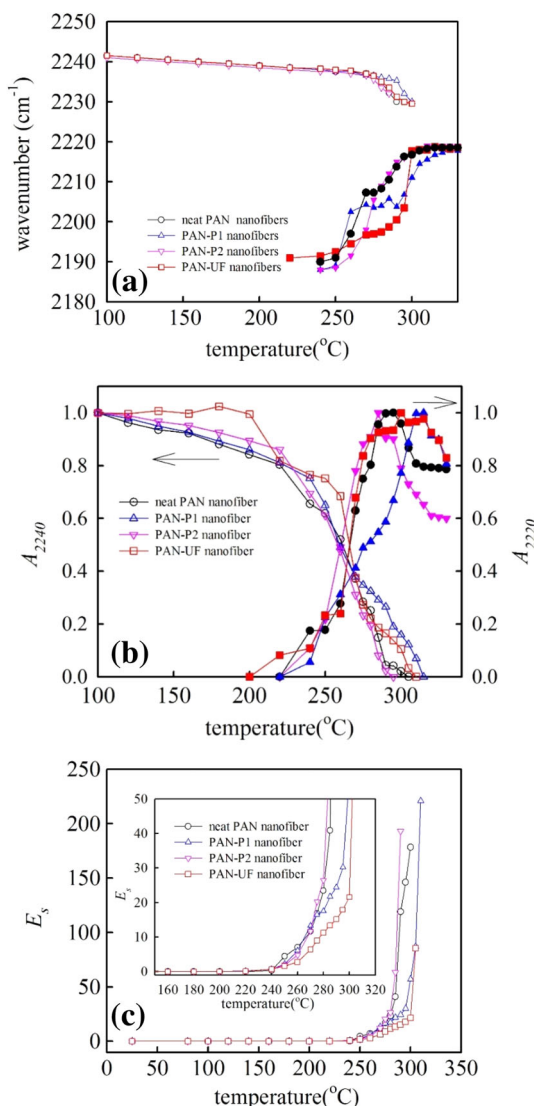


**Figure 4.** (a) variation in absorbance peak, (b) normalized area of the  $2240\text{ cm}^{-1}$  (open symbols denote  $A_{2240}$ ) and  $2220\text{ cm}^{-1}$  (filled symbols denote  $A_{2220}$ ) bands, and (c) extent of stabilization of the neat PAN, PAN-P1, PAN-P2, and PAN-UF nanofibers with temperature during stepwise heating. The inset shows the higher magnifications of Figure 4(c). [Color figure can be viewed at [wileyonlinelibrary.com](http://wileyonlinelibrary.com)]

PAN-P2, and PAN-UF nanofibers with temperature during stepwise heating.  $A_{2240}$  was used in the following equation:

$$A_{2240} = \frac{A_{2240,T}}{A_{2240,100}} \quad (2)$$

where  $A_{2240}$  is the relative intensity of the nitrile groups, and  $A_{2240,T}$  and  $A_{2240,100}$  are the areas of the  $2240\text{ cm}^{-1}$  bands at different temperatures and at  $100\text{ }^{\circ}\text{C}$ , respectively. The radiation of the nitrile group process was characterized by the decreased  $A_{2240}$ . The  $A_{2240}$  of the neat PAN nanofibers decreased gradually and then a sharp transition occurred from  $240$  to  $290\text{ }^{\circ}\text{C}$  and then disappeared at  $305\text{ }^{\circ}\text{C}$ . Similar decreases in  $A_{2240}$  were also observed in the PAN-P1, PAN-P2, and PAN-UF nanofibers with

increased temperature, and sharp transitions for the PAN-P1, PAN-P2, and PAN-UF nanofibers were detected at  $250$ – $270$ ,  $240$ – $285$ , and  $260$ – $280\text{ }^{\circ}\text{C}$ , respectively, and then disappeared at  $315$ ,  $295$ , and  $310\text{ }^{\circ}\text{C}$ , respectively. Notably, the  $A_{2240}$  values of the PAN-UF between  $100$  and  $200\text{ }^{\circ}\text{C}$  were larger than those of the neat PAN, PAN-P1, and PAN-P2. The PAN-UF nanofibers had a higher sharp transitions temperature range of radiation of the nitrile group than the other PAN nanofibers.

Figure 4(b) also shows the normalized area of the absorbance band between  $2220$  and  $2190\text{ cm}^{-1}$  ( $A_{2220}$ ) of the neat PAN, PAN-P1, PAN-P2, and PAN-UF nanofibers with temperature during stepwise heating.  $A_{2220}$  was used in the following equation:

$$A_{2220} = \frac{A_{2220,T}}{A_{2220,MAX}} \quad (3)$$

where  $A_{2220}$  is the relative intensity of the isolated nitriles or imine groups bonded with an aromatic structure, and  $A_{2220,T}$  is the areas of the  $2220\text{ cm}^{-1}$  bands at different temperatures.  $A_{2220,MAX}$  is the maximum area of the  $2220\text{ cm}^{-1}$  bands during stepwise heating. Thus, the aromatization of the ring of the ladder structure was characterized by the increased  $A_{2220}$ . The  $A_{2220}$  of the neat PAN nanofibers was increased gradually and then a sharp transition occurred from  $260$  to  $285\text{ }^{\circ}\text{C}$ . The saturated  $A_{2220}$  of the neat PAN nanofibers were at  $290\text{ }^{\circ}\text{C}$  and then decreased at  $300\text{ }^{\circ}\text{C}$ . Similar increases in  $A_{2220}$  were also observed in the PAN-P1, PAN-P2, and PAN-UF nanofibers with increased temperature, and sharp transitions for the PAN-P1, PAN-P2, and PAN-UF nanofibers were detected at  $250$ – $305$ ,  $250$ – $280$ , and  $250$ – $275\text{ }^{\circ}\text{C}$ , respectively. The saturated  $A_{2220}$  of the PAN-P1, PAN-P2, and PAN-UF nanofibers were at  $310$ ,  $280$ , and  $280\text{ }^{\circ}\text{C}$ , respectively, and then decreased at  $320$ ,  $290$ , and  $320\text{ }^{\circ}\text{C}$ , respectively. The decrease in  $A_{2220}$  values indicated that the ladder structures of the neat PAN, PAN-P1, PAN-P2, and PAN-UF nanofibers were not stable at high temperature range. This could be caused by the enormous exothermal heat generated during stabilization.

Figure 4(c) shows the extent of stabilization ( $E_s$ ) of the neat PAN, PAN-P1, PAN-P2, and PAN-UF nanofibers with temperature during stepwise heating.  $E_s$  was used in the following equation<sup>18,29,31</sup>:

$$E_s = \frac{I_{1590,T}}{I_{2240,T}} \quad (4)$$

where  $E_s$  is the extent of stabilization,  $I_{1590,T}$  is the intensity of the  $1590\text{ cm}^{-1}$  bands at different temperatures, and  $I_{2240,T}$  is the intensity of the  $2240\text{ cm}^{-1}$  bands at different temperatures. The absorption bands at  $1590$  and  $2240\text{ cm}^{-1}$  were related to the imine and nitrile groups, respectively. Thus, the  $E_s$  indicated the formation of ladder structures via intramolecular and intermolecular nitrile crosslink reactions. The  $E_s$  of the neat PAN nanofibers increased sharply during the transition from  $250$  to  $300\text{ }^{\circ}\text{C}$ . The  $E_s$  of the PAN-P1, PAN-P2, and PAN-UF nanofibers similarly increased as the temperature increased, and sharp transitions for the PAN-P1, PAN-P2, and PAN-UF nanofibers were detected at  $250$ – $310$ ,  $250$ – $290$ , and  $250$ – $305\text{ }^{\circ}\text{C}$ , respectively. Notably, the  $E_s$  of the PAN-UF nanofibers was smaller than that of the neat PAN, PAN-P1, and PAN-P2 nanofibers [the inset of Figure 4(c)]. This result indicated that the intramolecular and

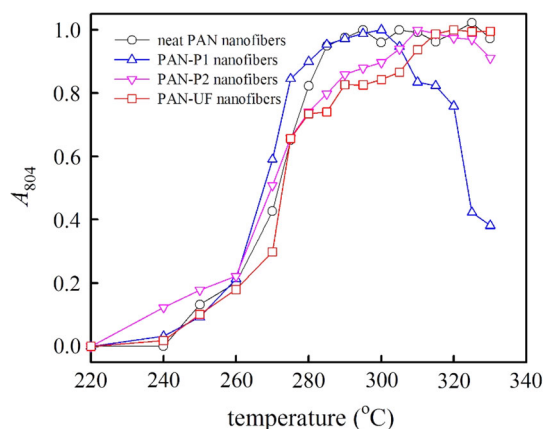


**Figure 5.** Normalized area of the  $804\text{ cm}^{-1}$  absorbance band ( $A_{804}$ ) of the neat PAN, PAN-P1, PAN-P2, and PAN-UF nanofibers with temperature during stepwise heating. [Color figure can be viewed at [wileyonlinelibrary.com](http://wileyonlinelibrary.com)]

intermolecular nitrile crosslink reactions of the PAN fibers with porous and ultrafine nanofibril structures were slower than those of the neat PAN nanofibers.

Figure 5 shows the normalized area of the absorbance band at  $804\text{ cm}^{-1}$  ( $A_{804}$ ) of the neat PAN, PAN-P1, PAN-P2, and PAN-UF nanofibers with temperature during stepwise heating.  $A_{804}$  was used in the following equation:

$$A_{804} = \frac{A_{804,T}}{A_{804,MAX}} \quad (5)$$

where  $A_{804}$  is the relative intensity of the triazine, and  $A_{804,T}$  are the areas of the  $804\text{ m}^{-1}$  bands at different temperatures.  $A_{804,MAX}$  is the maximum area of the  $804\text{ cm}^{-1}$  bands during stepwise heating. The intermolecular reaction of the nitrile group was characterized by the increase in  $A_{804}$ . The neat PAN nanofibers exhibited a significant increase in  $A_{804}$ , and a sharp transition occurred from 260 to 285 °C. Similar increases in  $A_{804}$  were also observed in the PAN-P1, PAN-P2, and PAN-UF nanofibers with increased temperature, and sharp transitions for the PAN-P1, PAN-P2, and PAN-UF nanofibers were detected at 260–275, 260–290, and 270–290 °C, respectively. Moreover, the  $A_{804}$  values of the PAN-P1 and PAN-P2 nanofibers decreased at 305 and 330 °C, respectively. The saturated  $A_{804}$  of the neat PAN and PAN-UF nanofibers were at 290 and 315 °C, respectively. Notably, the  $A_{804}$  values of the neat PAN, PAN-P1, and PAN-P2 nanofibers at 270 °C were higher than those of the PAN-UF nanofibers at 270 °C. The results implied that the intermolecular reaction of the nitrile group with adjacent nitrile for the PAN-UF nanofibers was more difficult than that for the neat PAN nanofiber, and that the triazine group of the PAN-P1 and PAN-P2 nanofibers would easily break down at a higher temperature range.

Based on above results, the PAN-P2 and PAN-UF nanofibers had poor thermal stabilities at high temperatures during heating. The poor thermal stabilities of PAN-P2 and PAN-UF nanofibers can be ascribed to their high surface area which allows the fast evolution of volatiles. The fast evolution of volatiles in the PAN-P2 and PAN-UF nanofibers cannot be absolutely excluded. However, another plausible source is that the orientation of the PAN chains in the PAN-P2 and PAN-UF nanofibers affects the

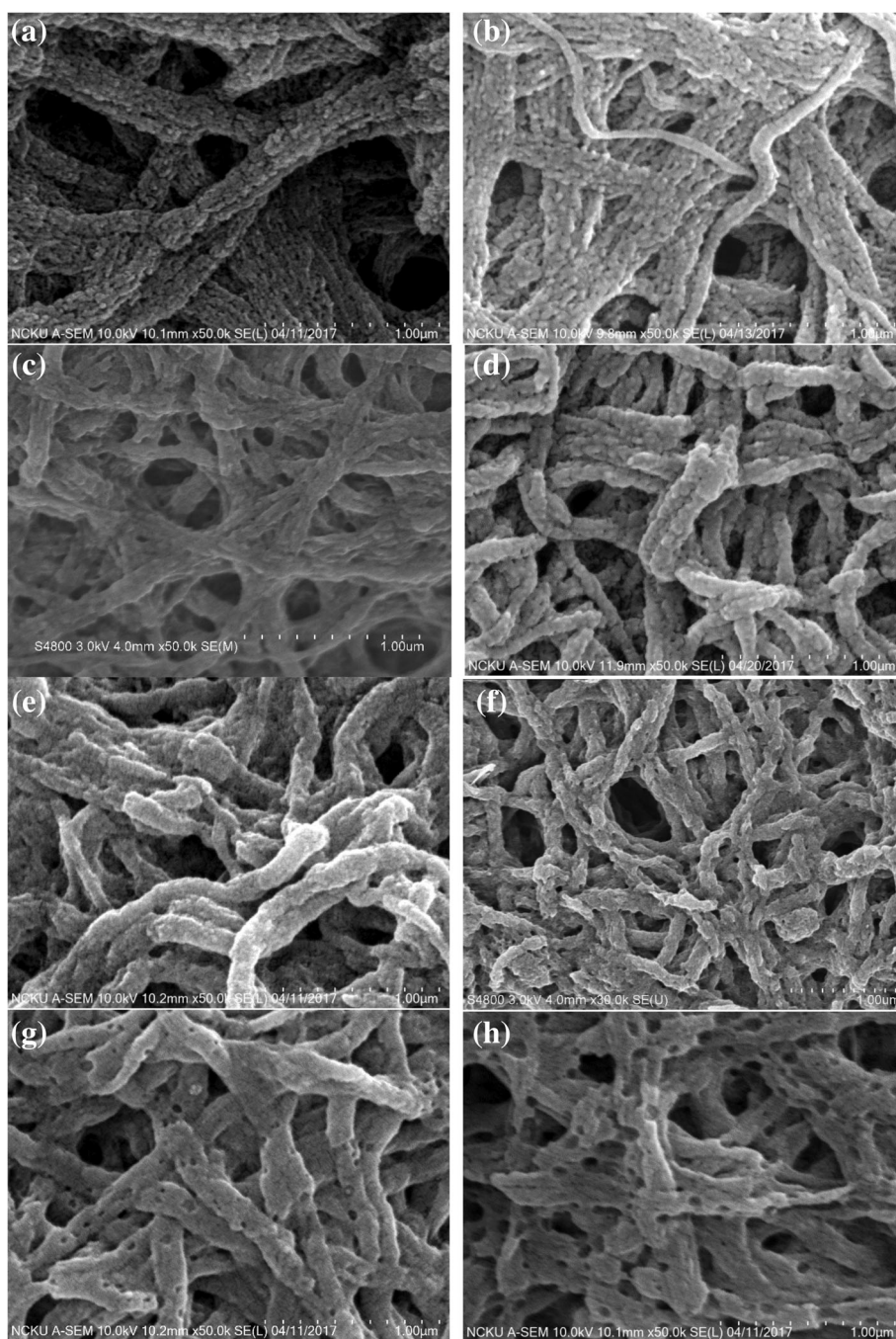
intermolecular and intramolecular reactions of the nitrile group. According to Lian *et al.*,<sup>20</sup> the cyclization index of the PAN chains in the PAN fiber decreases at the high stretching ratios of PAN fiber during thermal heating. The orientation of the PAN chains in the PAN-P2 and PAN-UF nanofibers exceed that of the neat PAN nanofibers, which may cause difficulty for the intramolecular cyclization reactions in the PAN-P2 and PAN-UF nanofibers. Therefore, the ladder structures of the PAN-P2 and PAN-UF nanofibers became unstable at high temperatures.

Figure 6 shows the SEM images of the PAN-UF nanofibers heated to different temperatures. After removing the PVP component in the PAN/PVP 25/75 nanofibers, there were numerous spaces and pores between the ultrafine nanofibrils. When the temperature increased to become greater than the  $T_g$  of PAN, the ultrafine nanofibers still could be observed, but the  $d_f$  of the ultrafine nanofibrils was increased. However, when the temperature increased to 200 °C, the ultrafine nanofibrils were hard to identify. When the temperature increased to 270 °C, the porous structures of the PAN-UF nanofibers could be observed.

Figure 7 shows the  $d_f$  of the neat PAN and PAN-UF nanofibers during heating. The  $d_f$  of the neat PAN nanofibers were not changed at approximately 420 nm until the temperature was higher than the  $T_g$  of PAN. When the temperature increased to 120 °C, the  $d_f$  of the neat PAN nanofibers was slightly increased to approximately 450 nm. This result indicated that the PAN nanofibers underwent thermal expansion because the PAN chains had mobility at temperature over its  $T_g$ . Moreover, when the temperature increased to 260 °C, the  $d_f$  of the neat PAN nanofibers began to decrease dramatically. Cipriani *et al.*<sup>17</sup> reported a similar result. This result revealed that the PAN nanofibers would experience thermal shrinkage during the PAN crosslinking and cyclization reactions.

The outer shell diameter of the PAN-UF nanofibers decreased as the temperature increased when the temperature became greater than the  $T_g$  of PAN. However, the  $d_f$  of the ultrafine nanofibrils increased as the temperature increased. This result indicated that the PAN chains in the ultrafine nanofibrils had the appropriate energy and mobility to close the pores left from thermal relaxation during thermal heating. Therefore, selecting a good stabilization temperature for ultrafine PAN-crosslinked nanofibrils was capable of enhancing the structure stability during thermal heating. The color of PAN-UF mats changed from white to brown, and the ultrafine nanofibril structures were changed dramatically during heating. Therefore, the mechanical property of PAN-UF mats would change, but the PAN-UF mats still showed flexible mats during heating to 320 °C. However, the real mechanical property of PAN-UF during heating was beyond the scope of this study and deserved future work.

Based on the above stepwise heating results, the intermolecular cyclization of the nitrile group could be significantly observed at 260 °C. In order to reduce the thermal relaxation of the PAN chains during thermal heating, an appropriate temperature for the intermolecular cyclization reaction of the nitrile group could improve the structure stability. Therefore, 260 °C was selected for isothermal heating. Figure S4 shows the FTIR spectra of the PAN-UF nanofibers during stepwise heating from 25 to 260 °C,



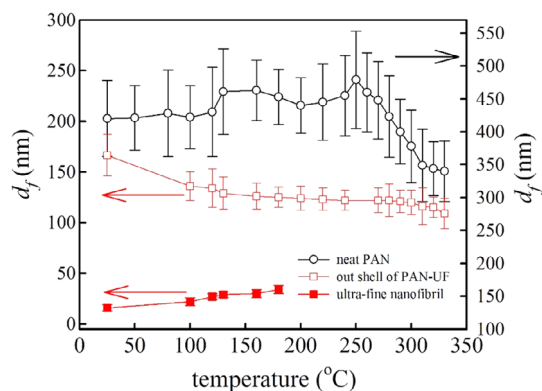
**Figure 6.** SEM images of PAN-UF nanofibers heated to (a) 100, (b) 160, (c) 180, (d) 200, (e) 240, (f) 260, (g) 270, and (h) 320 °C in air atmospheres at 1 °C min<sup>-1</sup>.

the subsequent isothermal heating at 260 °C for 5 h, and then stepwise heating from 260 to 330 °C. When the PAN-UF underwent isothermal heating at 260 °C for 5 h, the absorption bands at 2240 cm<sup>-1</sup> decreased with time, whereas the absorption bands at 1587 and 800 cm<sup>-1</sup> increased with time.

After isothermal heating, the absorption bands at 2240 and 804 cm<sup>-1</sup> for 5 h were significantly different from those for 0 min. Figure 8(a) shows the  $A_{2240}$  and  $A_{2220}$  of the neat PAN and PAN-UF nanofibers during isothermal heating at 260 °C for 5 h. During the isothermal heating at 260 °C, the  $A_{2240}$  value of

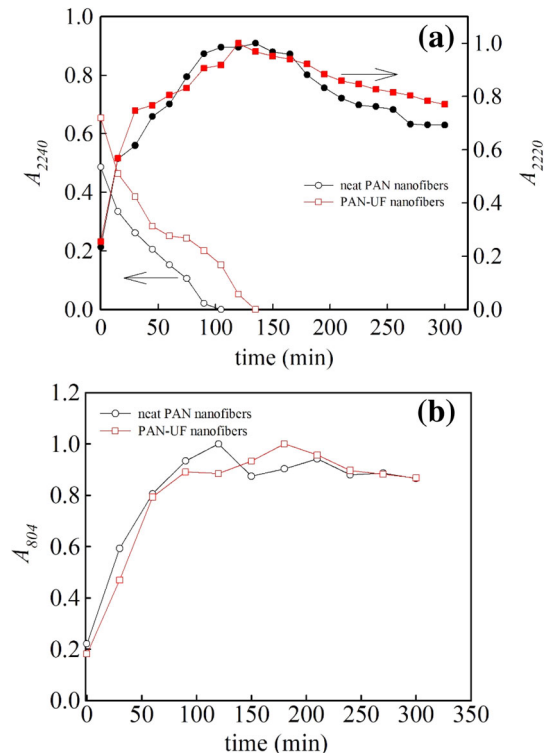
the neat PAN and PAN-UF nanofibers exhibited step drops from 0 to 75 min and from 0 to 45 min, respectively, and then disappeared at 105 and 135 min, respectively. The  $A_{2240}$  values of the neat PAN nanofibers were smaller than those of the PAN-UF nanofibers. On the other hand, the  $A_{2220}$  values of the neat PAN and PAN-UF nanofibers exhibited increases from 0 to 105 min and from 0 to 120 min, respectively, and then slightly decreased with time.

Figure 8(b) shows the  $A_{804}$  of the neat PAN and PAN-UF nanofibers during isothermal heating at 260 °C for 5 h. During



**Figure 7.** Fiber diameter of the neat PAN and PAN-UF nanofibers during heating. [Color figure can be viewed at wileyonlinelibrary.com]

the isothermal heating at 260 °C, the  $A_{804}$  values of the neat PAN and PAN-UF nanofibers exhibited sharp transitions from 0 to 90 min, which was then followed by a plateau. Moreover, the  $A_{804}$  values of the neat PAN and PAN-UF nanofibers showed the maximum value at 120 and 180 min, respectively, and then were slightly decreased during following heating. The  $A_{804}$  values of the neat PAN nanofibers are slightly larger than that of the PAN-UF nanofibers from 0 to 120 min. The results indicated that the intermolecular and intramolecular nitrile crosslink reactions for the PAN-UF nanofibers were slower than those for the neat PAN nanofibers during stepwise or isothermal heating.



**Figure 8.** (a) Normalized area of the 2240  $\text{cm}^{-1}$  ( $A_{2240}$ ) and 2220  $\text{cm}^{-1}$  ( $A_{2220}$ ) bands, and (b) normalized area of the 804  $\text{cm}^{-1}$  ( $A_{804}$ ) bands of the neat PAN and PAN-UF nanofibers with time during isothermal heating at 260 °C for 5 h. [Color figure can be viewed at wileyonlinelibrary.com]

### Carbonized Structures

According to the above results, stabilization and carbonization of the PAN-UF nanofibers were used in the following step. The PAN-UF nanofibers were heated to 260 °C in air for 2 h at a

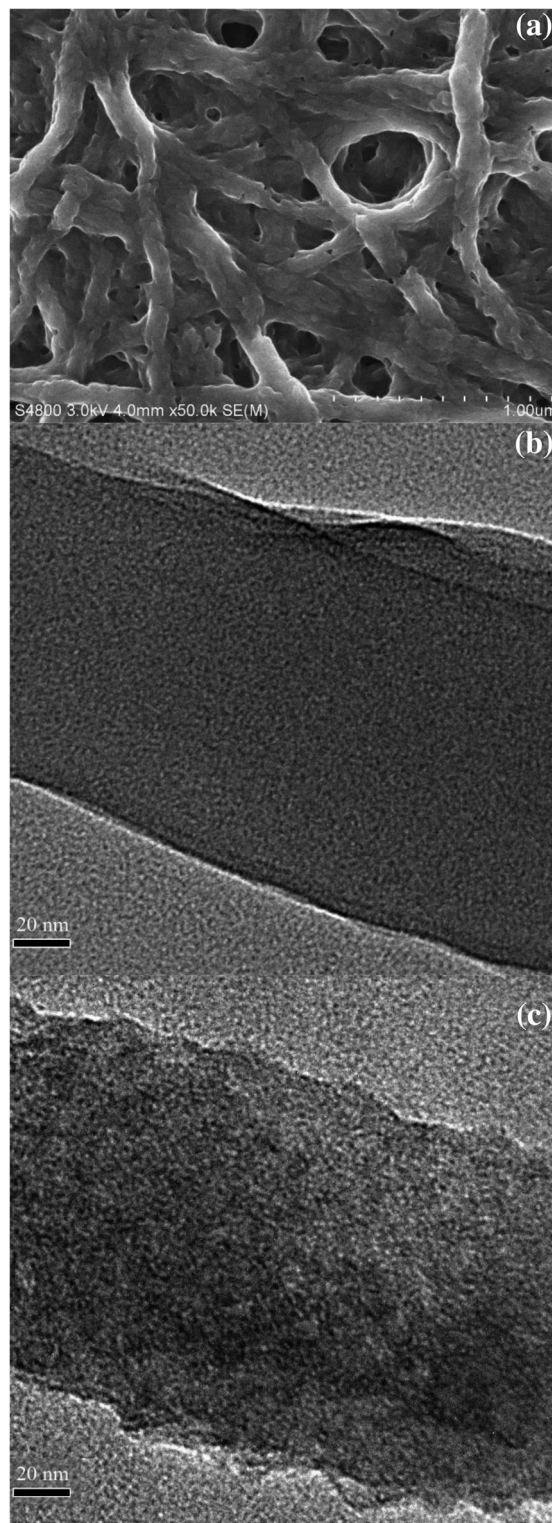


**Figure 9.** SEM images of (a) CNF-UF@260. TEM images of (b) CNF-UF and (c) CNF-UF@260.

**Table II.** Summary of the Crystal Structure Parameters and Surface Area of the Various Types of CNFs from WAXD

Sample code	$2\theta_{(002)}$ ( $^{\circ}$ )	$\beta$ (radian)	$L_c$ (nm)	Surface area ( $\text{m}^2 \text{g}^{-1}$ )
Neat CNF	24.85	0.124	1.146	11.6
CNF-P1	24.80	0.126	1.128	17.3
CNF-P2	24.30	0.128	1.109	9.8
CNF-UF	24.85	0.120	1.184	1.9
CNF-UF@260	24.86	0.116	1.225	96.0

heating rate of  $1^{\circ}\text{C min}^{-1}$  for the stabilization process, and subsequently heated to  $900^{\circ}\text{C}$  in a nitrogen atmosphere for 1 h at a heating rate of  $5^{\circ}\text{C min}^{-1}$  for the carbonization process. CNF-UF@260 was then obtained. Figure 9(a) shows SEM images of the CNF-UF@260 nanofibers. The  $d_f$  of CNF-UF@260 was  $74 \pm 12$  nm. Compared with the morphologies of CNF-UF, a porous structure could be observed in the CNF-UF@260. Moreover, the fiber diameter of CNF-UF@260 was about 0.64-fold smaller than that of CNF-UF. This result indicated that the surface area of the CNF-UF@260 was larger than that of the CNF-UF. Figure 9(b,c) shows the TEM images of the CNF-UF and CNF-UF@260 nanofibers. Compared with the morphologies of CNF-UF, a clearer turbostratic structure could be observed in the

CNF-UF@260 nanofibers. This result revealed that the CNF-UF@260 nanofibers had better carbon crystals than the CNF-UF nanofibers.

The BET surface area and pore size of the various types of CNF mats are listed in Table II. The neat CNF showed a small surface area of  $11.6 \text{ m}^2 \text{g}^{-1}$ , because the CNFs in this study were not oxidation etched with oxidizing gases (activation process). This BET surface area result was similar with those from the study of Miao *et al.*<sup>32</sup> The BET surface area values of the neat CNF, CNF-P1, and CNF-P2 mats were similar. Moreover, the BET surface area values of CNF-UF@260 were significantly larger than those of neat CNF, CNF-P1, CNF-P2, and CNF-UF. Notably, the BET surface area values of CNF-UF were the smallest, because the pore structure between ultrafine PAN nanofibrils would merge together during thermal heating. This was consistent with SEM results (Figure 6). Moreover, based on Figure S5(a), the SEM image of the cross section of CNF-UF showed dense structures without any fiber structures. This finding indicated that the nanofibrils inside the CNF-UF mats merged together. Figure S5 (b) shows the SEM image of the cross section of CNF-UF@260 with individual fibril structures. Although the  $d_f$  of CNF-UF@260 was only 0.64-fold smaller than that of CNF-UF, the inside structures of CNF-UF and CNF-UF@260 were crucially different. Thus, the surface area of CNF-UF is significantly smaller than that of neat CNF and CNF-UF@260.

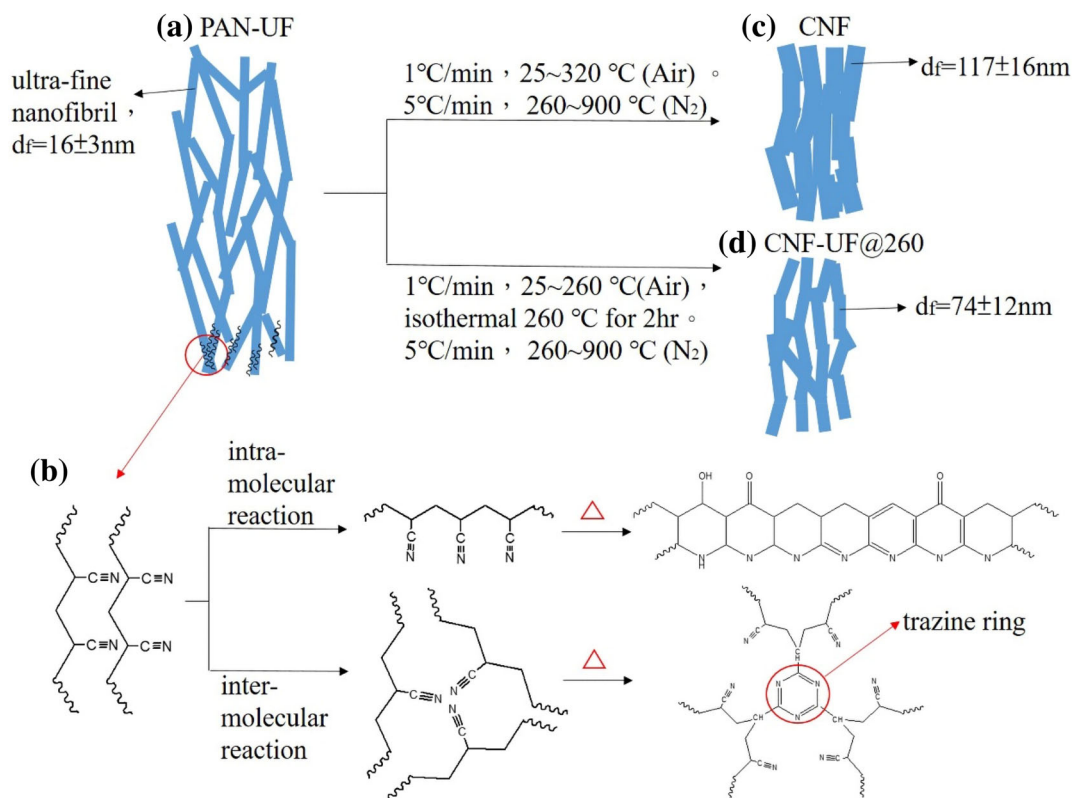


**Figure 10.** Schematic of the morphology change and intermolecular and intramolecular cyclization reactions of the PAN-UF nanofibers during the stabilization and carbonization processes. (a) the morphology of PAN-UF nanofibers, (b) the intermolecular and intramolecular (triazine ring) cyclization reaction routes of PAN polymer chains, (c) the morphology of CNF-UF, and (d) the morphology of CNF-UF@260. [Color figure can be viewed at [wileyonlinelibrary.com](http://wileyonlinelibrary.com)]

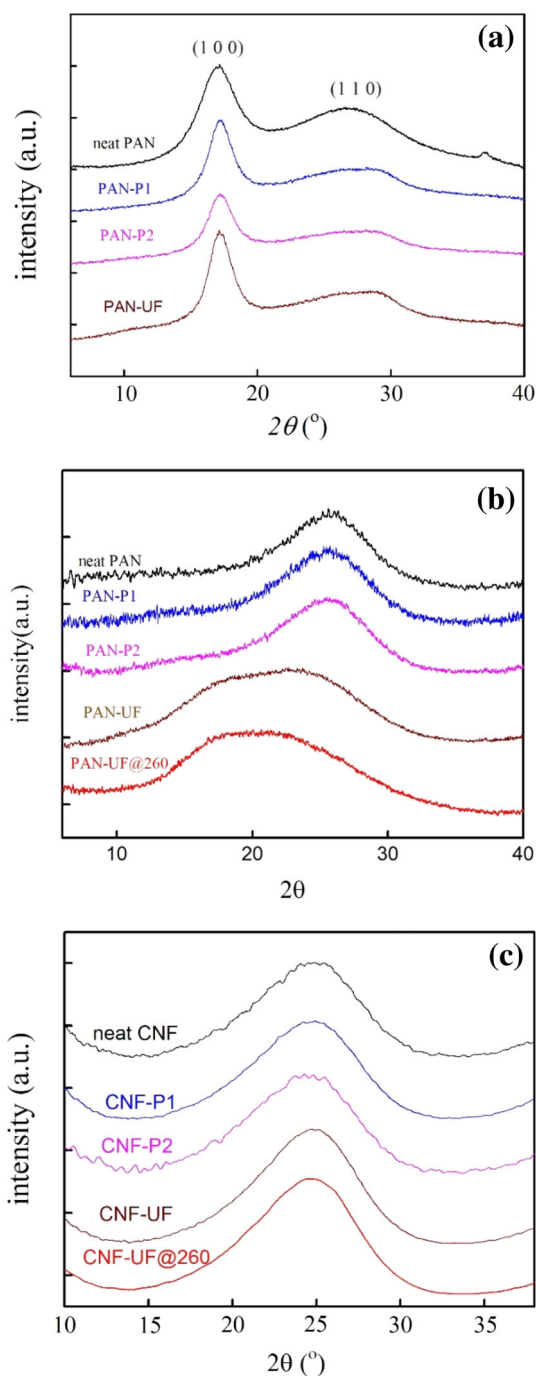


**Figure 11.** WAXD intensity of (a) PAN fibers with porous and ultrafine nanofibril structures, (b) PAN fibers with porous and ultrafine nanofibril structures after thermal stabilization, and (c) various types of CNFs. [Color figure can be viewed at [wileyonlinelibrary.com](http://wileyonlinelibrary.com)]

The morphology change and intermolecular and intramolecular cyclization reactions of the PAN-UF nanofibers during the stabilization and carbonization processes are illustrated in Figure 10. The ultrafine nanofibrils would merge together which cause the appropriate energy and mobility of PAN chains from thermal relaxation during thermal heating. When the ultrafine PAN nanofibrils underwent isothermal heating at 260 °C, the intramolecular reactions of the nitrile group in the ultrafine PAN nanofibrils would be

increased to enhance the structure stability after carbonization. According to Sun *et al.*,<sup>8</sup> the residue of PVP polymer chains for PAN-P1, PAN-P2, and PAN-UF nanofibers would crosslink with PAN polymer chains. However, the crosslinking reaction temperature between PAN and PVP polymer chains could be higher than the intramolecular reaction temperature of the nitrile group.<sup>24</sup> Moreover, the amount of PVP in the PAN-P1, PAN-P2, and PAN-UF nanofibers was too small to form sufficient crosslinking structure to limit the mobility of the PAN polymer chains. Therefore, the morphology difference between CNF-UF and CNF-UF@260 was mainly caused by intramolecular reactions of the nitrile group in the ultrafine PAN nanofibrils.

Figure 11(a) shows the WAXD intensity of the PAN fibers with porous and ultrafine nanofibril structures. The neat PAN nanofibers showed a strong diffraction peak at  $2\theta$  of 17.1° and a broad halo appeared between 21 and 30°, whereas the PAN-P1, PAN-P2, and PAN-UF nanofibers showed a strong diffraction peak at the  $2\theta$  of 17.1° and a weak diffraction at  $2\theta$  angle of 29°. These diffraction peaks were consistent with the results of Liu *et al.*<sup>25</sup> The diffraction peaks at  $2\theta$  of 17.1 and 29° were characteristic (100) and (110) reflections for the PAN hexagonal lattice. This result indicated that the crystalline and macromolecular orientations in the neat PAN nanofibers were lower than those in the PAN-P1, PAN-P2, and PAN-UF nanofibers.

Figure 11(b) shows the WAXD intensity of the PAN fibers with porous and ultrafine nanofibril structures after thermal stabilization. For the neat PAN, PAN-P1, and PAN-P2 nanofibers, the strong diffraction peaks at  $2\theta$  of 17.1° disappeared, and a diffraction peak appeared at  $2\theta$  of 25.6°, which corresponded to the (101) crystallographic plane and indicated the formation of aromatic ring or ladder structures, which was consistent with the results of Liu *et al.*<sup>25</sup> For the PAN-UF and PAN-UF@260 nanofibers, a broad halo appeared between 15 and 30° because the diffraction peak at  $2\theta$  of 17.1° decreased, and the diffraction peak at  $2\theta$  of 25.6° slightly increased. The WAXD results were consistent with the FTIR results and indicated that the PAN chains, which were confined in the ultrafine nanofibrils, were harder to form the aromatic ring or ladder structures during stabilization.

Figure 11(c) shows the WAXD intensity of the various types of CNFs. All types of CNFs showed a strong diffraction peak at about 24.8°, corresponding to the graphitic crystallite planes (002).<sup>9</sup> The lateral crystallite thickness ( $L_c$ ) of the various types of CNFs could be determined by the Scherrer equation, corresponding to the (002) reflection.<sup>9,11,33</sup>

$$L_c = \frac{0.9\lambda}{\beta \cos\theta} \quad (6)$$

where  $\lambda = 0.154$  nm is the wavelength of the Cu  $K_\alpha$  X-ray,  $\theta$  is the Bragg diffraction angle, and  $\beta$  is the full width at half maximum intensity in radians. The  $2\theta_{(002)}$ ,  $\beta$ , and  $L_c$  of the various types of CNFs are listed in Table II. The  $\beta$  of the CNF-P2 was larger than that of the other types of CNFs. Thus, the  $L_c$  of CNF-P2 was smaller than that of the other types of CNFs. The  $L_c$  of the CNF-UF@260 was larger than that of the CNF-UF. This result indicated that CNF-UF@260 had a better graphitic structure than the CNF-UF.

**Table III.** Electrical Conductivity and Specific Capacitance of the Various Types of CNF Mats

Sample	Electrical conductivity (S cm <sup>-1</sup> )	Specific capacitance (F g <sup>-1</sup> )
Neat CNF	0.37	6.53
CNF-P1	166.76	7.55
CNF-P2	188.30	11.26
CNF-UF	14.33	1.84
Neat CNF@260	121.50	6.80
CNF-UF@260	1000.72	31.00

### Electrical Properties

The electrical conductivity ( $\sigma$ ) values of the various types of CNF mats are listed in Table III. The CNF-P1, CNF-P2, and CNF-UF mats also had larger  $\sigma$  values than the neat CNF mats. This implied that the small amount of PVP, which was left over in the PAN-P1, PAN-P2, and PAN-UF nanofibers, helped to reduce the resistivity from the interfiber connection of the CNFs during carbonization. This result was similar to that of Niu *et al.*<sup>9</sup> This phenomenon cannot be absolutely excluded. However, the  $\sigma$  was also relative to the carbon structure of the CNFs. The  $\sigma$  of CNF-UF was 10-fold smaller than those of CNF-P1 and CNF-P2. The  $\sigma$  of CNF-UF@260 was significantly larger than those of CNF-UF and the neat CNF@260. Both CNF-UF and CNF-UF@260 had PVP to help the interfiber connection, and the  $L_c$  values of both CNF-UF and CNF-UF@260 were larger than those of the CNF-P1 and CNF-P2. Therefore, the larger differences in  $\sigma$  between CNF-UF and CNF-UF@260 were caused by the formation of the ladder structures during stabilization, which affected the carbonized structure of the CNF-UF and CNF-UF@260 during carbonization. This implied that the ladder structures of the PAN-UF nanofibers for stabilization at 260 °C had better ladder structures than that of the PAN-UF nanofibers for stabilization at 320 °C. The ladder structures of the PAN-UF nanofibers could be broken easily at high temperatures, which was consistent with the FTIR results.

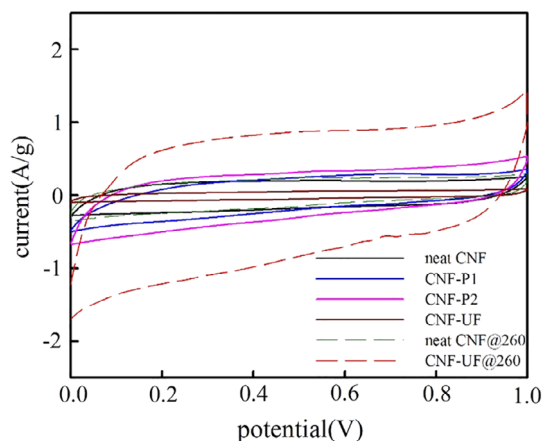


**Figure 12.** Electrochemical CV curves of various types CNF mats. [Color figure can be viewed at [wileyonlinelibrary.com](http://wileyonlinelibrary.com)]

Figure 12 shows the electrochemical CV curves of various types of CNF mats. All CNF membranes had a near-rectangular charge/discharge characteristic. The specific capacitances ( $C_m$ ) were calculated according to the CV curves (Figure 11).  $C_m$  was used in the following equation<sup>34</sup>:

$$C_m = \frac{\int IdV}{vm\Delta V} \quad (7)$$

where  $I$  is the response current (A),  $\Delta V$  is the voltage window (V),  $v$  is the scan rate (V s<sup>-1</sup>), and  $m$  is the weight (g).  $C_m$  value of the various types of CNFs is listed in Table III. The CNF-P1 and CNF-P2 also had larger  $C_m$  values than the neat CNF. However, the surface area values of neat CNF, CNF-P1, and CNF-P2 were similar. Thus, the larger  $C_m$  of the CNF-P1 and CNF-P2 could be attributed to the increase in electrical conductivity of the CNF-P1 and CNF-P2. Moreover, the neat CNF and neat CNF@260 had similar  $C_m$  values but vastly different  $\sigma$  values. The  $d_f$  values of neat CNF and neat CNF@260 were similar, which indicated that their the surface area of neat CNF and neat CNF@260 were also similar. Therefore, the  $\sigma$  of neat CNF@260 was higher than that of neat CNF, indicating that the graphitic structures of neat CNF@260 were better than those of neat CNF, although the improvement was insufficient to significantly increase  $C_m$  values. CNF-UF had the smallest  $C_m$  values of any types among CNF, whereas CNF-UF@260 had the largest capacitance value of 31.00 F g<sup>-1</sup>. This phenomenon was due to the synergistic effects of the large surface area and good graphitic structures in CNF-UF@260. This result indicated that the stabilization temperature for ultrafine PAN nanofibrils would affect the structure of the CNF and then influence the performance of the CNF electrode.

### CONCLUSIONS

PAN fibers with porous and ultrafine nanofibril structures were prepared by electrospinning a PAN/PVP phase separation solution and then the selectively removing the PVP component from the electrospun PAN/PVP bicomponent nanofibers. The PAN fibers with porous and ultrafine nanofibril structures subsequently carried out air stabilization and nitrogen carbonization processes to prepare the CNFs for electrode application. The effects of the PAN fiber structures on the stabilization process were investigated using several analytical techniques, including TGA, DSC, FTIR, WAXD, SEM, and TEM. Furthermore, the possible electrode application in a supercapacitor was evaluated by CV. According to the FTIR results, the intermolecular and intramolecular reactions of the nitrile group for the PAN fibers with ultrafine nanofibril structures exhibited slower reaction rates than those for the neat PAN nanofibers during stepwise and isothermal heating. This indicated that the PAN chains, which were confined in the ultrafine nanofibrils, were harder to form the aromatic ring or ladder structures during stabilization. The ladder structure of the crosslinked PAN chains for the PAN fibers with porous and ultrafine nanofibril structures could easily break down at higher temperatures. Thus, the microstructure of the PAN fibers with porous and ultrafine nanofibril structures could affect the intermolecular and intramolecular reactions of the

nitrile group during stabilization. Moreover, the ultrafine PAN nanofibrils would merge together during the stabilization process, because the PAN chain of the ultrafine PAN nanofibrils had the appropriate energy and mobility to close the pores left from thermal relaxation during thermal heating. The surface area and carbonized structure of the PAN fibers with porous and ultrafine nanofibril structures were affected after carbonization. In order to obtain the high surface area of CNF, selecting a good stabilization temperature for the ultrafine PAN-crosslinked nanofibrils to crosslink was capable of enhancing the structure stability during thermal heating. Based on the FTIR results, the temperature of 260 °C was selected for stabilization for 2 h. The carbonized structure, surface area, and conductivity of the CNF-UF@260 mats were better than those of the CNF-UF, neat CNF, and neat CNF@260 mats. Moreover,  $C_m$  of the CNF-UF@260 mats was fourfold higher than that of the neat CNF@260 mats. CNFs with porous and ultrafine nanofibril structures are of interest for electrode application in energy storage.

#### ACKNOWLEDGMENTS

The authors would like to thank the Ministry of Science and Technology of Taiwan for the research grant (MOST 104-2221-E-035-081-) and (MOST 105-2632-E-035-001-) which supported this work, respectively. The authors appreciate the Precision Instrument Support Center of Feng Chia University for providing the measurement facilities.

#### REFERENCES

- Pandolfo, A.; Hollenkamp, A. *J. Power Sources*. **2006**, *157*, 11.
- Wang, Y.; Wang, Z.; Yu, X.; Li, B.; Kang, F.; He, Y.-B. *J. Mater. Res.* **2018**, *33*, 1058.
- Li, Z.; Zhang, J.-W.; Yu, L.-G.; Zhang, J.-W. *J. Mater. Sci.* **2017**, *52*, 6173.
- Wang, X.; Ding, B.; Yu, J.; Wang, M. *Nano today*. **2011**, *6*, 510.
- Inagaki, M.; Yang, Y.; Kang, F. *Adv. Mater.* **2012**, *24*, 2547.
- Zhang, L.; Hsieh, Y.-L. *Nanotechnology*. **2006**, *17*, 4416.
- Zhang, Z.; Li, X.; Wang, C.; Fu, S.; Liu, Y.; Shao, C. *Macromol. Mater. Eng.* **2009**, *294*, 673.
- Sun, D.; Qin, G.; Lü, M.; Wei, W.; Wang, N.; Jiang, L. *Carbon*. **2013**, *63*, 585.
- Niu, H.; Zhang, J.; Xie, Z.; Wang, X.; Lin, T. *Carbon*. **2011**, *49*, 2380.
- Peng, M.; Li, D.; Shen, L.; Chen, Y.; Zheng, Q.; Wang, H. *Langmuir*. **2006**, *22*, 9368.
- Shilpa; Das, S. K.; Afzal, M. A. F.; Srivastava, S.; Patil, S.; Sharma, A., *Carbon* **2016**, *108*, 135.
- Bognitzki, M.; Frese, T.; Steinhart, M.; Greiner, A.; Wendorff, J. H.; Schaper, A.; Hellwig, M. *Polym. Eng. Sci.* **2001**, *41*, 982.
- Lee, S.; Moon, G. D.; Jeong, U. *J. Mater. Chem.* **2009**, *19*, 743.
- Rahaman, M. S. A.; Ismail, A. F.; Mustafa, A. *Polym. Degrad. Stab.* **2007**, *92*, 1421.
- Nataraj, S. K.; Yang, K. S.; Aminabhavi, T. M. *Prog. Polym. Sci.* **2012**, *37*, 487.
- Dalton, S.; Heatley, F.; Budd, P. M. *Polymer*. **1999**, *40*, 5531.
- Cipriani, E.; Zanetti, M.; Bracco, P.; Brunella, V.; Luda, M. P.; Costa, L. *Polym. Degrad. Stab.* **2016**, *123*, 178.
- Moskowitz, J. D.; Wiggins, J. S. *Polym. Degrad. Stab.* **2016**, *125*, 76.
- Lai, C.; Zhong, G.; Yue, Z.; Chen, G.; Zhang, L.; Vakili, A.; Wang, Y.; Zhu, L.; Liu, J.; Fong, H. *Polymer*. **2011**, *52*, 519.
- Lian, F.; Liu, J.; Ma, Z.; Liang, J. *Carbon*. **2012**, *50*, 488.
- Servaty, R.; Schiller, J.; Binder, H.; Kohlstrunk, B.; Arnold, K. *Bioorg. Chem.* **1998**, *26*, 33.
- Frank, E.; Steudle, L. M.; Ingildeev, D.; Spörl, J. M.; Buchmeiser, M. R. *Angew. Chem. Int. Ed. Engl.* **2014**, *53*, 5262.
- Lei, S.; Cao, W.; Fu, Z.; Xu, L. *J. Appl. Polym. Sci.* **2016**, *133*, 43890.
- Kim, H. S. *J. Polym. Sci. Part B: Polym. Phys.* **1996**, *34*, 1181.
- Liu, J.; Zhou, P.; Zhang, L.; Ma, Z.; Liang, J.; Fong, H. *Carbon*. **2009**, *47*, 1087.
- Fochler, H.; Mooney, J.; Ball, L.; Boyer, R.; Grasselli, J. *Spectrochim. Acta Part A*. **1985**, *41*, 271.
- Lin-Vien, D.; Colthup, N. B.; Fateley, W. G.; Grasselli, J. G. *The Handbook of Infrared and Raman Characteristic Frequencies of Organic Molecules*; Elsevier: New York, **1991**. p. 277.
- Qin, X.; Lu, Y.; Xiao, H.; Song, Y. *Mater. Lett.* **2012**, *76*, 162.
- Collins, G.; Thomas, N.; Williams, G. *Carbon*. **1988**, *26*, 671.
- Jing, M.; Wang, C.-G.; Wang, Q.; Bai, Y.-J.; Zhu, B. *Polym. Degrad. Stab.* **2007**, *92*, 1737.
- Arbab, S.; Mirbaha, H.; Zeinolebadi, A.; Nourpanah, P. *J. Appl. Polym. Sci.* **2014**, *131*, 40343.
- Miao, F.; Shao, C.; Li, X.; Wang, K.; Liu, Y. *J. Mater. Chem. A*. **2016**, *4*, 4180.
- Kim, B.-H.; Yang, K. S. *J. Ind. Eng. Chem.* **2014**, *20*, 3474.
- Zhou, W.; Zhou, K.; Liu, X.; Hu, R.; Liu, H.; Chen, S. *J. Mater. Chem. A*. **2014**, *2*, 7250.